

LABORATORY EXERCISES

EVAN DAVID WELLMEYER

M.Sc. Atmospheric Science and Technology

Lab of Atmospheric Remote Sensing

Dr. Annalisa Di Bernardino

Dr. Marco Cacciani

Dr. Monica Campanelli

Università Degli Studi Dell'Aquila, L'Aquila

Sapienza Università Di Roma, Rome

2021

1 Analysis of Turbulence from Sonic Anemometer

The Eddy-Covariance Method (ECM) is the only method that allows the direct determination of the main parameters that describe the turbulence of the PBL. A ground-based weather station that allows the use of the ECM method must have a fast response sensor that measures the three wind components (u, v, w) and potential air temperature (θ) . The main sensor normally used in an ECM station is the tri-axial ultrasonic anemometer. An ECM station must also be equipped with an interrogation and acquisition system of elementary measurements at a high sampling frequency (10-20 Hz).

The ECM method is presented in the following way: suppose we consider a flat and regular site in which the current lines of the air flow are regular (parallel to the surface and straight) and we measure the three components of the wind vector (u, v, w) and the virtual potential temperature (θ_v) over an averaging period T . The averaging period must be long enough to allow a statistically correct estimate of the variances and covariances, but also sufficiently short to allow the overall state of the PBL to be considered stationary. The wind vectors and other quantities must be measured with maximum possible precision by ideal sensors of zero order. The wind must be measured with respect to an orthogonal Cartesian reference system. At each instant t , belonging to the averaging period T , each variable of interest (u, v, w, θ) can be considered the sum of an average value and a turbulent fluctuation, according to the Reynolds decomposition.

$$u(t) = \bar{u} + u'(t) \quad (1.1)$$

In the averaging period T , N measurements will be available for each variable corresponding to the time instants $t_0 + \Delta t, t_0 + 2\Delta t, \dots, t_0 + N\Delta t$. If N is high enough, we can calculate the following:

Standard deviation for a generic variable α :

$$\sigma_\alpha = \sqrt{\frac{1}{N-1} \sum_{k=1}^N [(\alpha_k - \bar{\alpha})^2]} \quad (1.2)$$

Covariance between two generic variables α and β

$$\overline{\alpha'\beta'} = \frac{1}{N-1} \sum_{k=1}^N [(\alpha_k - \bar{\alpha}) \cdot (\beta_k - \bar{\beta})] \quad (1.3)$$

where

$$\bar{\alpha} = \frac{1}{N} \sum_{k=1}^N \alpha' \quad \text{and} \quad \bar{\beta} = \frac{1}{N} \sum_{k=1}^N \beta' \quad (1.4)$$

Except very close to the ground, the horizontal shear stress is supported by macroscopic turbulent motion. When parcels of air travel vertically, they exchange momentum between layers of air with different velocities.

Vertical gradients in horizontal mean velocity lead to changes in instantaneous horizontal velocities during this transfer of momentum. During situations where turbulence is generated or modulated by wind shear near the ground, the magnitude of the surface Reynolds' stress is an important scaling variable. The total vertical flux of horizontal momentum measured near the surface is

$$\tau_{xz} = -\overline{\rho u' w'_s} \quad \text{and} \quad \tau_{yz} = -\overline{\rho v' w'_s}$$

$$|\tau_0| = [\tau_{xz}^2 + \tau_{yz}^2]^{1/2}$$

These arguments suggest that the turbulent velocities are associated with shear production of turbulence scale with surface friction velocity, u_* , defined as

$$u_* \equiv \sqrt{\frac{\tau_0}{\rho}} = \left[\overline{u' w'_s}^2 + \overline{v' w'_s}^2 \right]^{1/4} \quad (1.5)$$

which has the dimension of velocity and integrates the shear stress in the flow. In order to estimate the friction velocity it is necessary to compute the covariances between the horizontal components and vertical component of wind.

Another important parameter characteristic of the PBL is the turbulent sensible heat flux H_0 , which is the transfer of heat caused by the difference in temperature between the ground (or sea) and the air. This is calculated as

$$H_0 = \rho C_p \overline{w' \theta'} \quad (1.6)$$

where ρ is the air density and C_p is the specific heat at constant air pressure.

Buoyant and shear production of turbulence operate together to determine the structure of the boundary layer. The Monin-Obukhov Length is a scaling parameter that is useful in the surface layer to describe the effects of buoyancy and shear on turbulent flows, particularly in the lower tenth of the atmospheric boundary layer. The absolute value of the Monin-Obukhov length, L , is roughly the height at which the turbulent velocity generated by shear is equal to that which is produced by buoyancy:

$$u_* \approx u_f(z = L) = \left(\frac{g}{T_0} Q_0 L \right)^{1/3}$$

where u_f is the free convection velocity scale and Q_0 is the kinematic heat flux. The Monin-Obukhov length L is calculated as follows:

$$L = -\frac{\overline{\theta_v}}{kg} \frac{u_*^3}{\overline{w' \theta'}} \quad (1.7)$$

where θ_v is the average virtual potential temperature, k is the von Karman constant and g is the acceleration due to gravity. L is usually negative in the daytime since $w' \theta'$ is typically positive during the day over land, and L is usually positive at nighttime when $w' \theta'$ is typically negative. L typically becomes infinite at dawn and dusk when the value of $w' \theta'$ passes through zero. So L is positive when the boundary layer is stable, and negative when it is unstable. Additionally, shear production of turbulence dominates that by buoyancy at heights below the Monin-Obukhov length, while buoyant production becomes dominant above it. It is possible to quantify the dispersion capabilities of the ambient atmosphere according to atmospheric stability classes according to the value of the Monin-Obukhov length as shown in Table 1.1.

Stability class	Obukhov length range
A	$-40 < L < 0$
B	$-200 < L < -40$
C	$-500 < L < -200$
D	$ L > 500$
E	$200 < L < 500$
F	$100 < L < 200$
G	$40 < L < 100$
H	$0 < L < 40$

Table 1.1: Classification of Holtslag in eight atmospheric stability classes. (Holtslag et al., 2016)

Taking the average standard deviation of the vertical wind component, $\overline{\sigma_w}$, the turbulent intensity I for an averaging period can be calculated

$$I \equiv \frac{\overline{\sigma_w}}{\overline{u}} \quad (1.8)$$

which quantifies the stationarity of the phenomenon.

Using data from a sonic anemometer recording at 32 Hz (2764800 samples per day) in Rome during April 19-20, 2018, the aforementioned variables may be calculated according to chosen averaging periods (aggregation bins) T . The chosen aggregation bins are 1h, 6h, 12h and 24h. The preliminary component velocity values for these aggregation bins for the two days are in Figure 1.2.

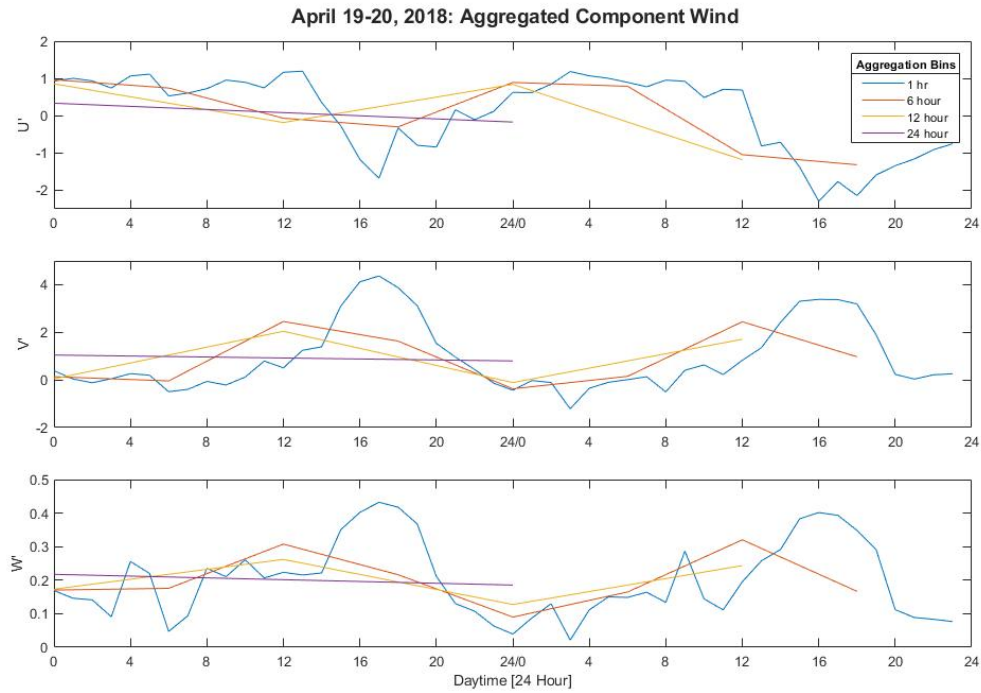


Figure 1.1

Figure 1.2: Wind component values for the aggregation bins during April 19 and 20, 2018.

The timeseries of 1h aggregation binned velocity components show a significant variation in all wind components between 15h and 20h on both April 19 and 20, with a clear diurnal cycle for aggregation bins up to 12h in length. The potential temperature timeseries for the aggregation bins (Figure 1.3) shows the diurnal cycle with decent resolution for all time bins up to 12h.

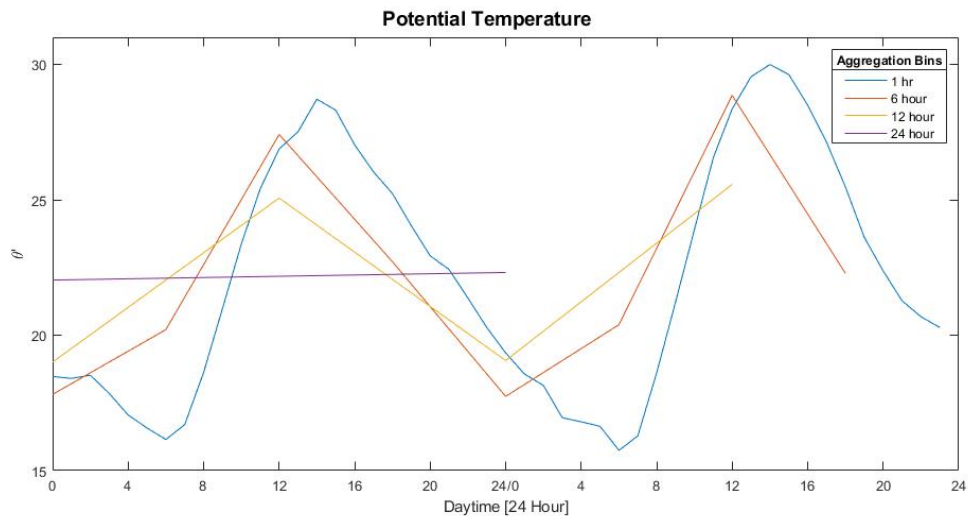


Figure 1.3: Potential temperature for the aggregation bins during April 19 and 20, 2018.

Calculating the covariances between the fluctuations in the wind components, the friction velocity u_* is calculated for the various aggregation bins for the two days as seen in Figure 1.4. Maximum values for friction velocity in the 1h aggregation bin timeseries are correlated with late afternoon maximum values for wind velocity component fluctuations, signifying the increased shear stresses contribute to the growing PBL. Friction velocity values for the 6h aggregation bin is able to resolve the peak in the mid-late afternoon; however, magnitudes reflected for across the different aggregation bins are drastically different for the common times.

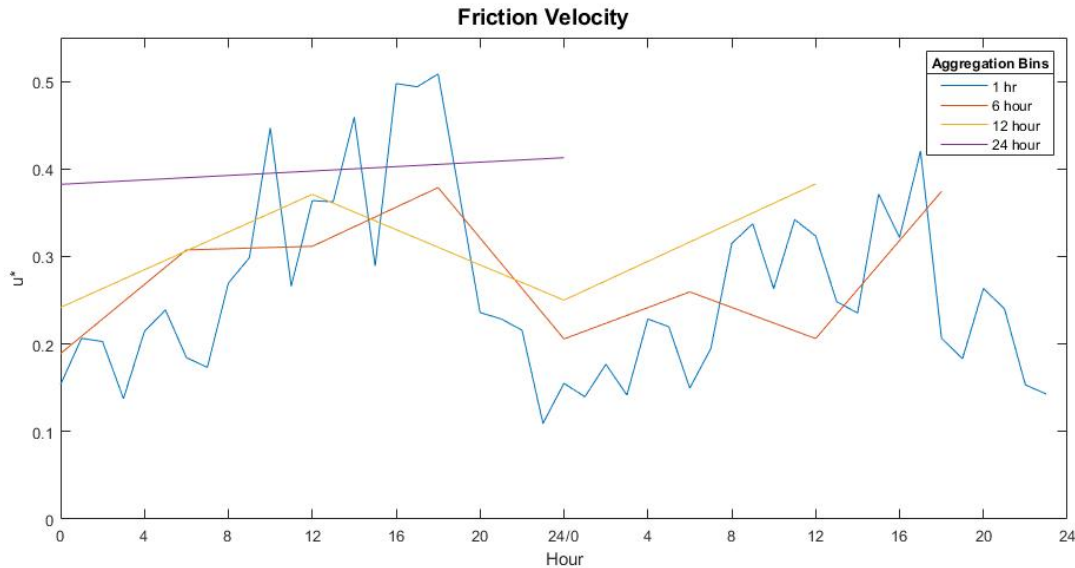


Figure 1.4: Friction velocity for the aggregation bins during April 19 and 20, 2018.

The value obtained by multiplying the fluctuating component (Equation 1.1) of the vertical velocity with the fluctuating component of the potential temperature is called the turbulent flow of heat. The turbulent flow of heat calculations for the various aggregation bins are in Figure 1.5, which shows the vertical transport of heat due to turbulent motion peaking in the mid-late afternoon.

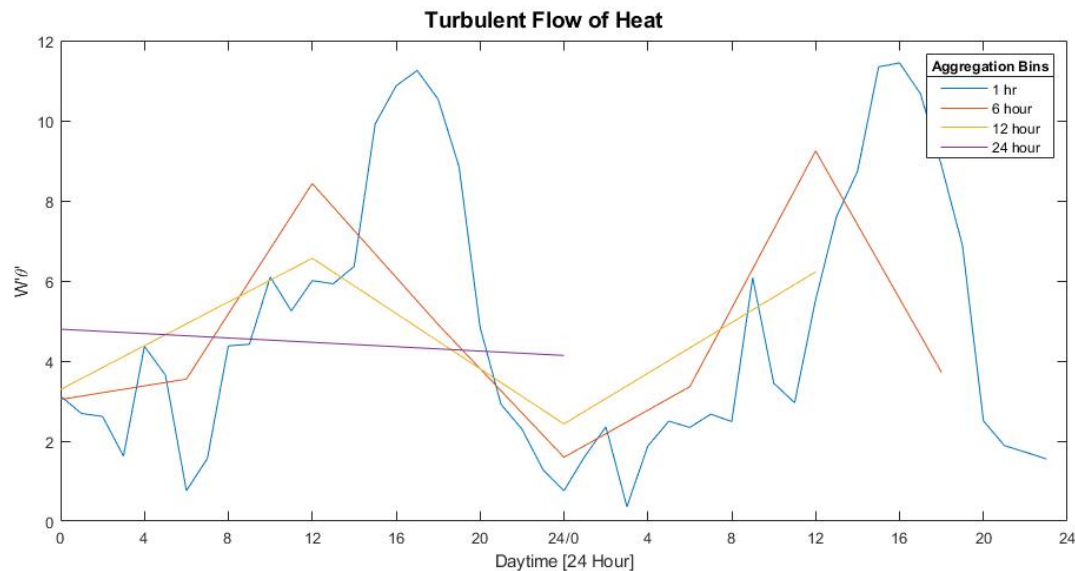


Figure 1.5: Turbulent flow of heat for the aggregation bins during April 19 and 20, 2018.

Multiplying the zonal wind fluctuation with the vertical wind fluctuation, the turbulent flow of momentum is obtained. The turbulent flow of momentum calculations for the various aggregation bins are in Figure 1.6. During the diurnal cycle, there is a significant transfer in the turbulent flow of momentum from $u'w'$ to $v'w'$ beginning in the early afternoon and peaking around 1700.

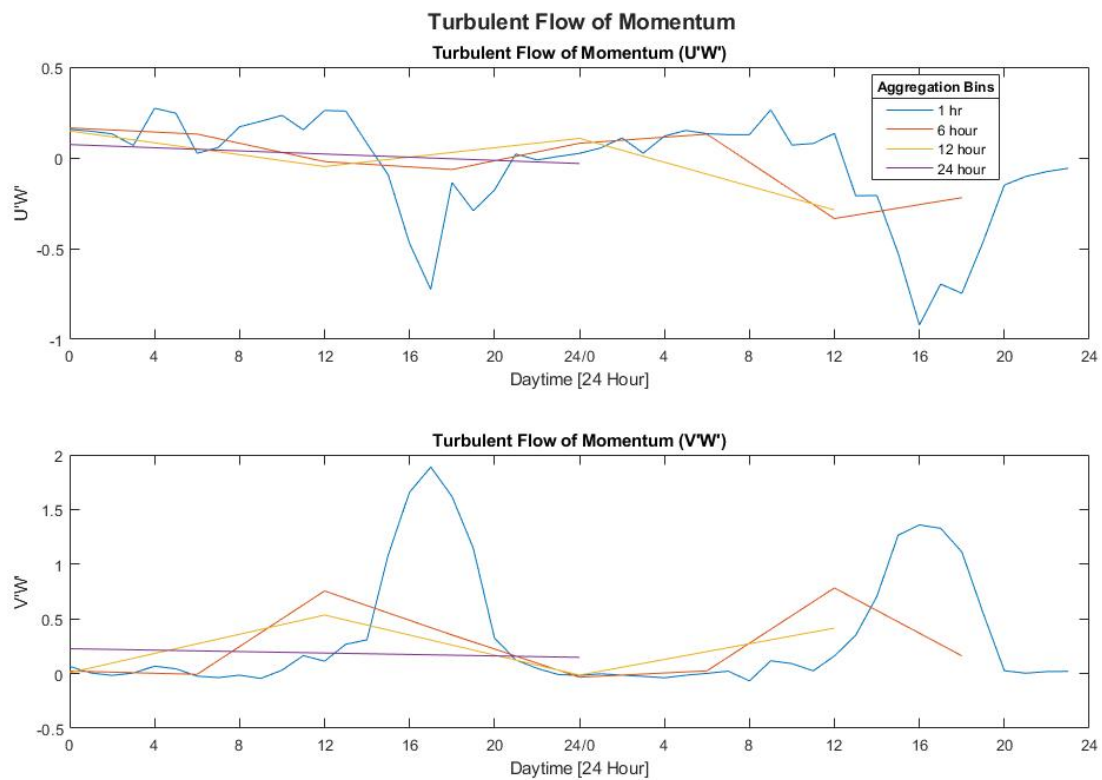


Figure 1.6: Turbulent flow of momentum for the aggregation bins during April 19 and 20, 2018.

By applying the vertical wind velocity and potential temperature to Equation 1.3, the result obtained may be used to calculate the turbulent sensible heat flux with Equation 1.6. The turbulent sensible heat flux calculations for the various aggregation bins are in Figure 1.7.

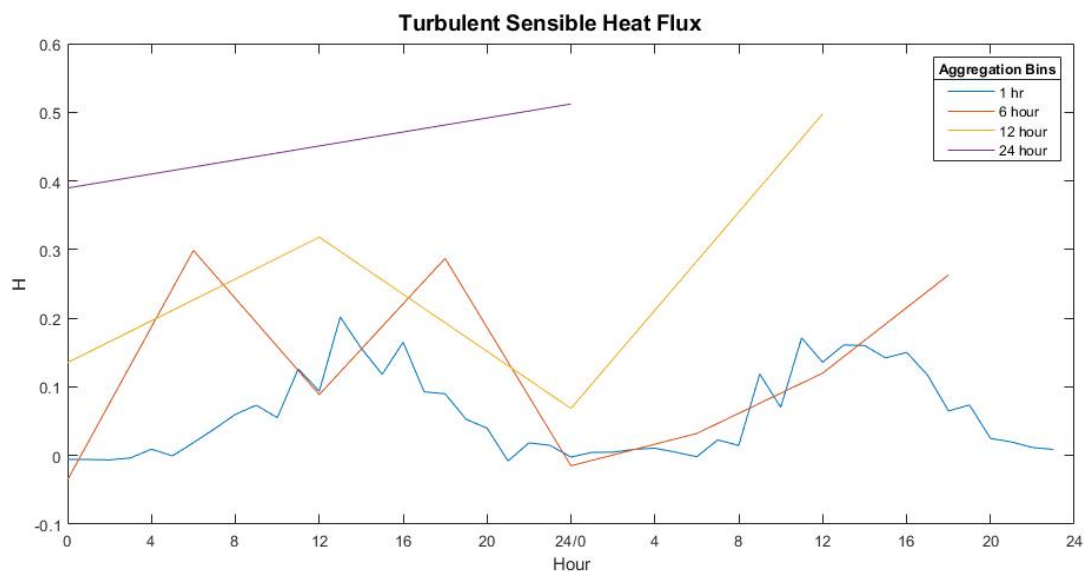
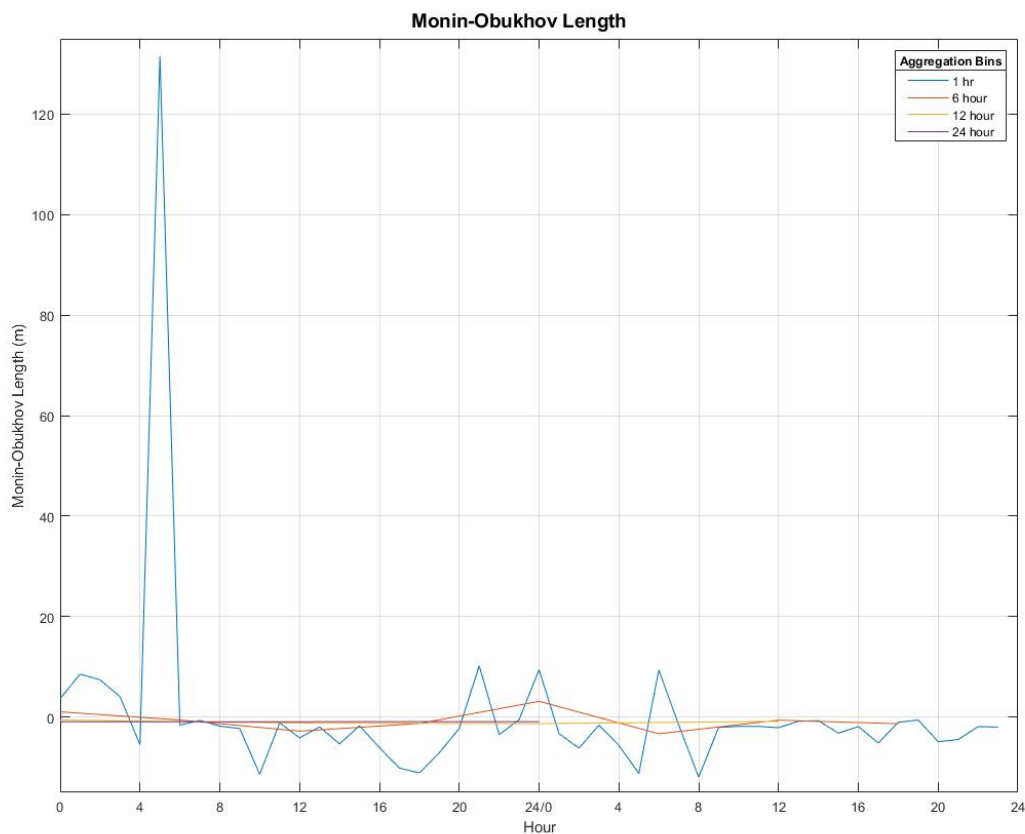
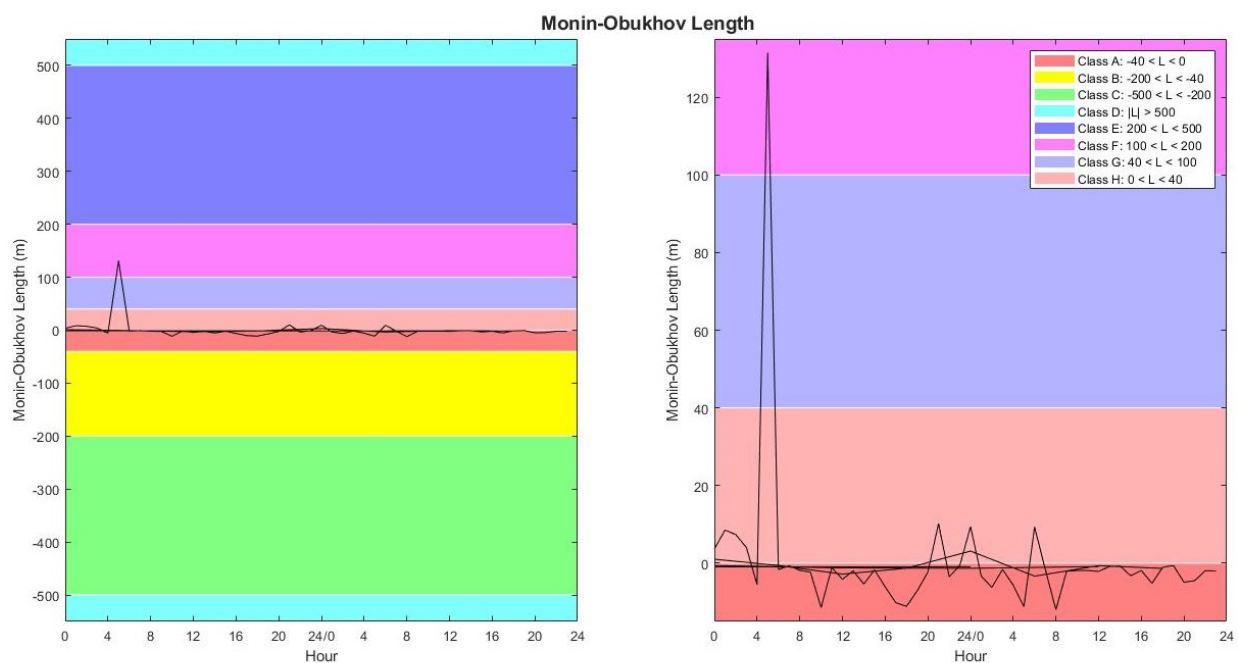


Figure 1.7: Turbulent sensible heat fluxes for the aggregation bins during April 19 and 20, 2018.

The turbulent sensible heat flux quantifies the transport of heat via turbulent mixing. Comparing the time-series of the various temporal bins, there is a clear difference in the resulting value for the turbulent sensible heat flux. The larger time bins result in larger values for the respective bins, due to the presence of larger fluctuations inside the bins that result in a larger value for the covariance.



(a)



(b)

Figure 1.8: Monin-Obukhov length for the aggregation bins during April 19 and 20, 2018. (Top) Panel (a) shows the Monin-Obukhov length for the respective aggregation bins by color code. (Bottom) Panel (b), left, shows the Monin-Obukhov length timeseries for all aggregation bins in perspective to all atmospheric stability classes (Table 1.1) and panel (b), right, shows the Monin-Obukhov length timeseries for all aggregation bins in perspective to only relevant stability classes.

Using previous calculations for the friction velocity and covariance of vertical wind and potential temperature, the Monin-Obukhov length was then calculated according to Equation 1.7. Figure 1.8a shows the Monin-Obukhov length for the respective aggregation bins by color code. Figure 3.4c, left, shows the Monin-Obukhov length timeseries for all aggregation bins in perspective to all atmospheric stability classes (Table 1.1) and Figure 3.4c, right, shows the Monin-Obukhov length timeseries for all aggregation bins in perspective to only relevant stability classes. The large spike in length on the morning of the 19th visible in the 1h aggregation timeseries is due to the large value generated by the equation as $w'\theta'$ approaches zero. The probability that a value of $w'\theta'$ nearing zero is included in the calculation of the Monin-Obukhov length increases as the aggregation time decreases (giving statistical significance to the small value within that time bin). Averaging the values of each respective aggregation length, the stability classes may be calculated. The stability classifications for each aggregation length for each day is present in Table 1.2.

Aggregation time	April 19, 2018	April 20, 2018
1 hour	Class H	Class A
6 hour	Class A	Class A
12 hour	Class A	Class A
24 hour	Class A	Class A

Table 1.2: Stability classifications of April 19 and 20, 2018 for different aggregation lengths, according to the Holtslag eight atmospheric stability classes. (Holtslag et al., 2016)

The turbulent intensity calculations are present in Table 1.3, showing the stationarity is consistent across time aggregation bins.

Aggregation time	April 19, 2018	April 20, 2018
1 hour	1.16	-2.18
6 hour	1.25	-2.29
12 hour	1.27	-2.36
24 hour	1.32	-2.46

Table 1.3: Turbulent intensity values of April 19 and 20, 2018 for different aggregation lengths.

2 Analysis of LIDAR Signal

The LIDAR signal is acquired at discrete time intervals starting from the pulse emission. The delay between the emission of the pulse and the acquisition of the signal at the time t_i corresponds at the altitude above the system. Each time interval (Δt) corresponds to an altitude interval.

$$z_i = \frac{ct_i}{2} \implies \Delta z = \frac{c\Delta t}{2}$$

The LIDAR record is a sequence of signals originating at a distance z_i that increases with an altitude step of Δz :

$$P_i = P(Z_i) = \frac{C_0}{(z_i - z_0)^2} [\beta_{mol}(z_i) + \beta_{aer}(z_i)] \exp \left\{ -2\Delta z \sum_{j=1}^{N_i} [\alpha_{mol}(z_j) + \alpha_{aer}(z_j)] \right\}$$

where N is the number of altitude intervals (altitude bins). The altitude vector is created using the altitude interval (vertical resolution)

$$z_i = (i - 1)\Delta z + z_0$$

where z_0 is the instrument altitude. Molecular backscattering and extinction coefficients can be estimated using observed or climatological profiles of atmospheric pressure and temperature from Rayleigh scattering theory. Vertical profiles of temperature, pressure, humidity and wind obtained by radiosounding were used in this case. The Rayleigh theory provides the value of the molecular backscattering coefficient obtained from the atmospheric molecular number density

$$\beta_m = n_m \sigma_m \quad (2.1)$$

where σ_m is the molecular backscattering cross section, that depends only on the wavelength of the incident radiation and does not depend on altitude

$$\sigma_m = \frac{d\sigma}{d\Omega} = 5.45 \cdot 10^{-32} \left[\frac{0.55}{\lambda} \right]^4 \quad (2.2)$$

where λ is in μm . It is possible to calculate the atmospheric molecular number density (molecules per cubic meter) using the ideal gas law

$$n_m(z) = \frac{P(z)}{k_B T(z)} \approx n_0 \exp\left\{-\frac{z}{H}\right\} \quad (2.3)$$

Since they are obtained by observations with a different vertical resolution, the values of n_m are not known at the same levels of the LIDAR signal. Taking the linear interpolation of $\log n_m(z) = -\frac{z}{H} + \log n_0$ allows to calculate the molecular profile at the LIDAR levels z_i

$$\beta_{mol}(z_i) = n_m(z_i) \sigma_m \quad (2.4)$$

Following then the Raleigh approach, the molecular extinction coefficient is linked to the backscattering coefficient by the equation

$$\beta_{mol}(z_i) = k_m \alpha_{mol}(z_i) \quad (2.5)$$

where k_m is the molecular backscattering-to-extinction ratio, independent on altitude

$$k_m = \frac{3}{8\pi} \quad (2.6)$$

The molecular extinction coefficient is then

$$\alpha_m = \frac{\beta_m}{k_m} \quad (2.7)$$

The previous variables can then be used to calculate the background noise via a synthetic signal. Some acquisition systems are able to acquire the detector signal before the pulse emission, thus providing the background noise immediately. However the alternative is take the far-field signal, where the contribution from the laser is negligible and use it to estimate the background contribution. Where the aerosol contribution to the LIDAR signal is negligible, the LIDAR signal is equal to

$$P_i = \frac{C_0}{(z_i - z_0)} [\beta_{mol}(z_i)] \exp\left\{-2\Delta z \sum_{j=1}^{N_m} [\alpha_{mol}(z_j) + \alpha_{aer}(z_j)]\right\} \exp\left\{-2\Delta z \sum_{j=1}^{N_m} [\alpha_{mol}(z_j)]\right\} + BKGD \quad (2.8)$$

where N_m is the altitude bin from where the aerosol contribution is negligible. The first exponential is the 2-way transmission where the aerosol is present and the second in the range without aerosol. If we define

$$T_0^2 \equiv \exp\left\{-2\Delta z \sum_{j=1}^{N_m} [\alpha_{mol}(z_j) + \alpha_{aer}(z_j)]\right\} = const. \quad (2.9)$$

allowing the LIDAR equation to be rewritten as

$$P_i = \frac{C_0 T_0^2}{(z_i - z_0)} [\beta_{mol}(z_i)] \exp\left\{-2\Delta z \sum_{j=1}^{N_m} [\alpha_{mol}(z_j)]\right\} + BKGD \quad \text{for } i \geq N_m \quad (2.10)$$

The molecular synthetic signal can then be calculated as

$$P_{m,i} = \frac{1}{(z_i - z_0)} [\beta_{mol}(z_i)] \exp\left\{-2\Delta z \sum_{j=N_m}^{N_i} [\alpha_{mol}(z_j)]\right\} \quad (2.11)$$

so in the no-aerosol range the LIDAR signal can be written in linear form $y = Ax + B$

$$P_i = [C_0 T_0^2] P_{m,i} + BKGD \quad (2.12)$$

the background can then be obtained using a linear fit with

$$A = C_0 T_0^2, \quad \boxed{B = BKGD}, \quad y = P_i, \quad x = P_{m,i} \quad (2.13)$$

Using the LIDAR signal, the altitude vector and the background noise, the Range Corrected Signal (RCS) can then be calculated

$$RCS_i \equiv (P_i - BKGD)(z_i - z_0)^2 = C_0[\beta_{mol}(z_i) + \beta_{aer}(z_i)] \exp \left\{ -2\Delta z \sum_{j=1}^{N_i} [\alpha_{mol}(z_j) + \alpha_{aer}(z_j)] \right\} \quad (2.14)$$

Using the Klett method, we can calculate the aerosol extinction coefficient by first converting the RCS expression into the following continuous function

$$Z(x) = Ay(x) \exp \left\{ -2 \int y(x') dx' \right\} \quad (2.15)$$

where A is an arbitrary constant. This is a Bernoulli equation (aka Ricatti Homogeneous Equation) with the solution

$$y(x) = \frac{Z(x)}{A - 2 \int Z(x') dx'} \quad (2.16)$$

From the molecular backscattering-to-extinction ratio and the equivalent for aerosol

$$k_m = \frac{\beta_m(z)}{\alpha_m(z)} = \frac{3}{8\pi} \quad k_a(z) = \frac{\beta_a(z)}{\alpha_a(z)} \quad (2.17)$$

we can write the backscattering coefficients as a function of extinction coefficients

$$\beta(z) = \beta_m(z) + \beta_a(z) = k_m \alpha_m(z) + k_a \alpha_a(z) \quad (2.18)$$

and

$$\alpha(z) = \alpha_m(z) + \alpha_a(z) \quad (2.19)$$

If we define $a(z) \equiv \frac{k_m}{k_a(z)}$, we can generate the transformation function

$$Y(z) = C' \frac{1}{k_a(z)} \exp \left\{ -2 \int_{z_m}^z \alpha_m(z') [a(z') - 1] dz' \right\} \approx C' \frac{1}{k_a} \exp \left\{ -2\Delta z \sum_{j=z_m}^{z_i} \alpha_{m,j} [a_j - 1] \right\} \quad (2.20)$$

where z_m is an altitude where the contribution of aerosol is negligible and C' has an arbitrary value. Multiplying by the RCS equation and simplifying we have

$$Z(z) = RCS(z)Y(z) = C_0 C' T_0^2 [a(z)\alpha_m(z) + \alpha_a(z)] \exp \left\{ -2\Delta z \sum_{j=z_m}^z [a_j \alpha_{m,j} + \alpha_{a,j}] \right\} \quad (2.21)$$

Defining the following

$$\alpha_w(z) \equiv a(z)\alpha_m(z) + \alpha_a(z) \quad (2.22)$$

$$C \equiv C_0 C' T_0^2$$

we have an equation of the Bernoulli form

$$Z(z) = C \alpha_w(z) \exp \left\{ -2\Delta z \sum_{j=z_m}^z \alpha_{w,j} \right\} \quad (2.23)$$

with the following solution for α_w

$$\alpha_w(z_i) = \frac{Z(z_i)}{C - 2\Delta z \sum_{j=N_m}^{N_i} Z(z_j)} \quad (2.24)$$

Following some rearranging and substitution, the solution for the aerosol extinction coefficient is therefore obtained

$$\alpha_a(z_i) = \frac{Z(z_i)}{C - 2\Delta \sum_{j=N_m}^{N_i} Z(z_j)} - \frac{k_m}{k_a(z_i)} \alpha_m(z_i) \quad (2.25)$$

The aerosol backscattering coefficient is then

$$\beta_a(z) = k_a(z) \alpha_a(z) \quad (2.26)$$

Data was obtained from the LiDAR system UNIROMA1-RAP recorded on the 10 May, 2021 at 10 min intervals from 05:00-20:50—making 96 profiles during the day. The LiDAR emission and detection wavelength was at 1064 nm at 5000 kHz, giving a vertical resolution of 3.75m. Light collection was done via 200mm Cassegrain telescope. Atmospheric profiles were obtained via the twice daily radiosounding at LIRE station, downloaded from the University of Wyoming.

The molecular backscattering cross section was first approximated according to emission wavelength with Equation 2.24. Using the pressure and temperature data obtained from the atmospheric sounding, the molecular number density was calculated using Equation 2.3 at both 00z and 12z times. The number density with height was then interpolated to the LiDAR heights via an interpolation function. The molecular backscattering coefficient with height was then calculated using Equation 2.4 and subsequently the molecular extinction coefficient using Equation 2.7. The results for the molecular backscattering and extinction coefficients calculated using the radiosounding data at both 00z and 12z are present in Figure 2.1.

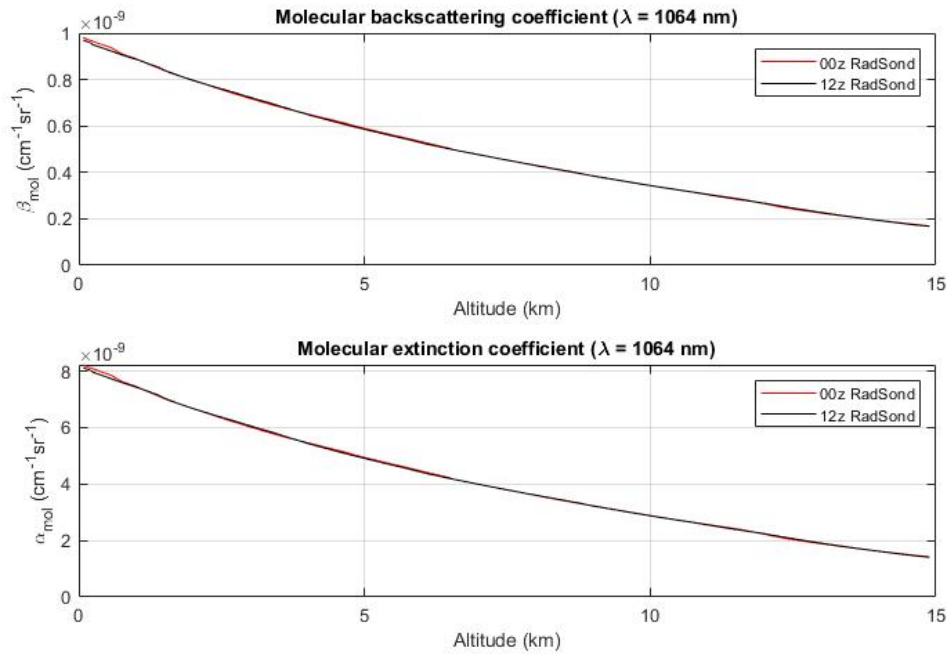


Figure 2.1: Molecular backscattering coefficient

Due to the nearly identical values for the molecular backscattering and extinction coefficients at the two times, only one sounding profile and subsequent coefficient calculations were used in the rest of the calculations for simplicity. Using the calculated molecular coefficients, the molecular synthetic signal was then calculated using Equation 2.11. Selecting the part of the synthetic and LiDAR signal above 10km, where aerosol contribution is negligible, a linear fitting function was used providing the background contribution as well as the values for $C_0 T_0^2$ (Equation 2.13). The derived background contribution to the LiDAR signal throughout the day (at each time) is presented as a timeseries in Figure 2.2. The background timeseries shows there is a large diurnal fluctuation in background noise throughout the day, peaking before noon, with subsequent peaks at approximately 14:30 and 15:30.

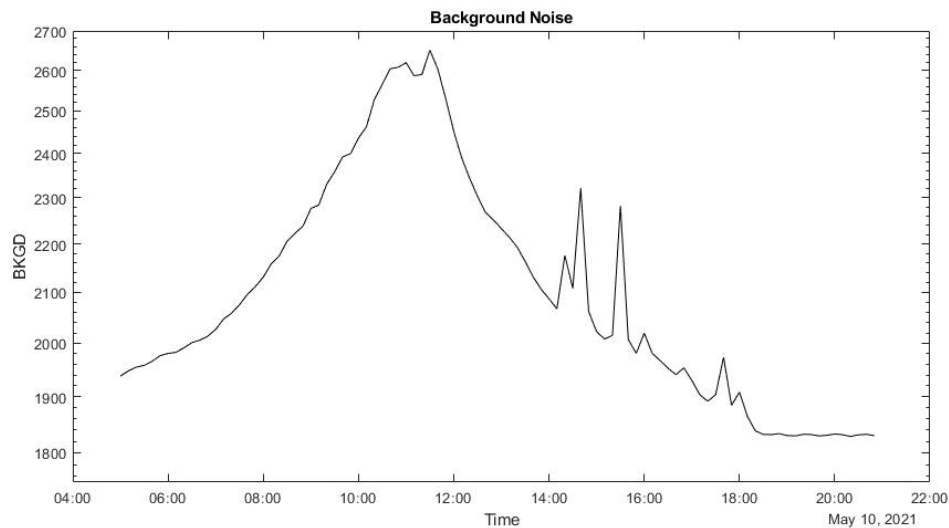


Figure 2.2: Background noise timeseries prenet in the LiDAR signal obtained from the linear fit of the synthetic signal with the LiDAR signal above 10km.

The synthetic LiDAR signal was recalculated according to Equation 2.12. The Range Corrected Signal (RCS) was then calculated according to Equation 2.14. Figure 2.3 shows both the signal and synthetic signal with the background noise removed (left) and the range corrected LiDAR and synthetic signal (right) for a single LiDAR profile at 17:40 when there is a large signal at approximately 10km altitude. Between the two plots in Figure 2.3, the range correction offers roughly 8 orders of magnitude increase in the signal.

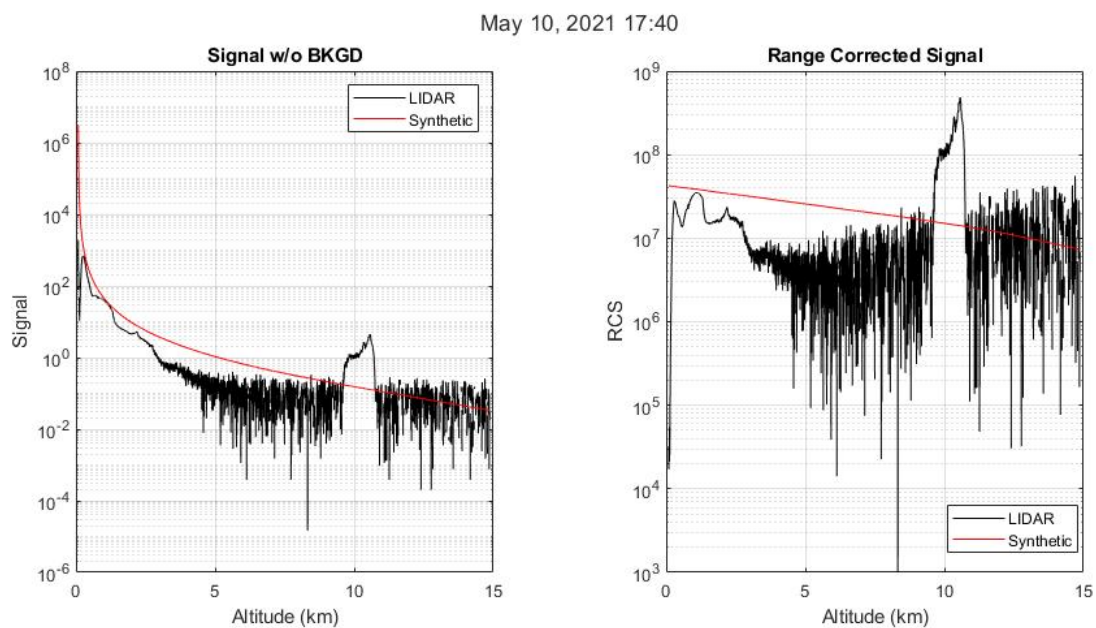


Figure 2.3: LiDAR and synthetic signal with background noise removed: left, normal signal; right, range corrected signal.

By repeating the process for each LiDAR profile collected throughout the day, the RCS can be presented as a cross section as in Figure 2.4, with altitude (km) as the y-axis and time of the day on the x-axis. The RCS is represented in color as the real part of the natural log of the RCS. Figure 2.4 contains two panels, which differ only in the altitude limits (y-axis), allowing analysis of upper level phenomena with greater vertical limits (top), and better analysis of near surface phenomena with restricted vertical limits (bottom). The LiDAR signal in the lower part of the atmosphere, as seen most clearly in the bottom panel of Figure 2.4, is attributed to the aerosol contained within the boundary layer. It is also clear from the RCS that the altitude of the boundary layer changes throughout the day, carrying the aerosols with it. In the late afternoon there is a large intensity of the signal from 8-10 km, which is attributed to high level clouds.

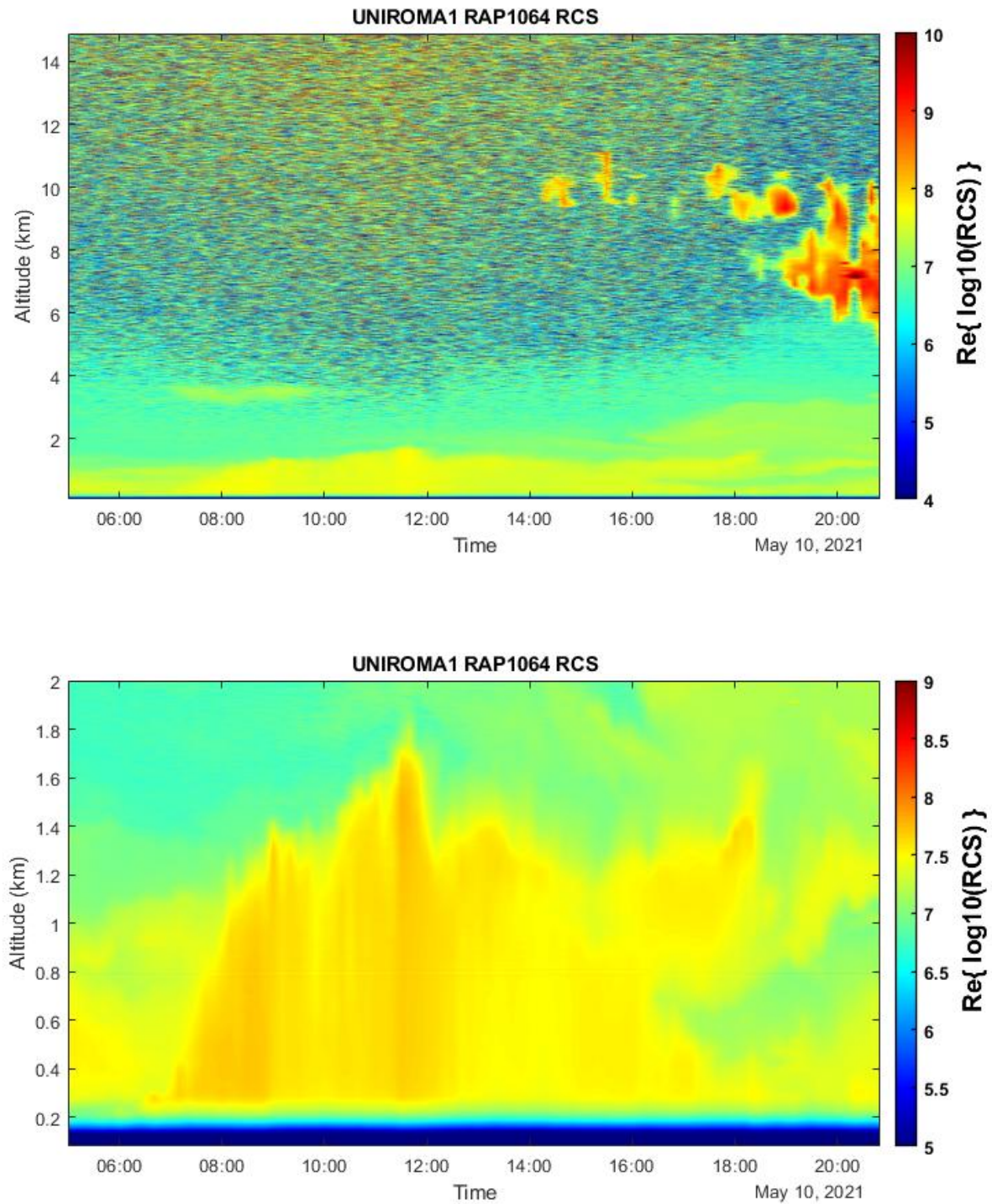


Figure 2.4: Range Corrected Signal for May 10, 2021 in Rome, Italy. The two panels are nearly identical and differ only in the altitude limits for visual aid of phenomena at various levels.

Once the RCS has been obtained, the Z function can be calculated via the discrete form of the Y function in Equation 2.20-2.21. The Z function is then used to calculate the aerosol extinction coefficient α_a according to Equation 2.25. The aerosol backscattering coefficient is then calculated via the aerosol backscattering-to-extinction coefficient. Figure 2.5 shows both a single LiDAR profile of the aerosol extinction coefficient, as well as the full cross section. The aerosol backscattering coefficient is not included in the figure as it relates to the extinction coefficient through a multiplication factor.

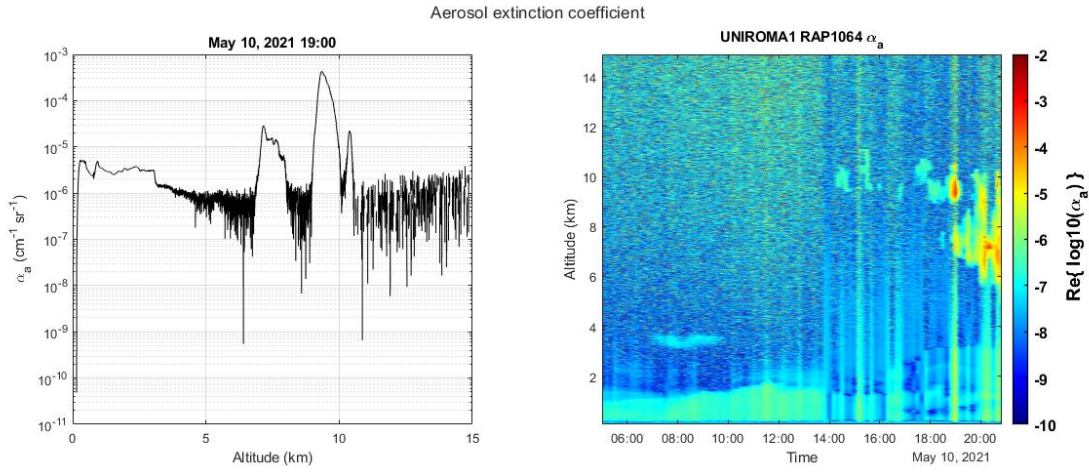


Figure 2.5: Calculated aerosol extinction coefficient for (left) a single profile at 05:00 and (right) the full day.

3 Photometer Aerosol Optical Depth and Volume Size Distribution

Atmospheric aerosols are a complex and dynamic mixture of solid and liquid particles from natural and anthropogenic sources. Different aerosols scatter or absorb sunlight to varying degrees depending on their physical properties, which are a direct effect of these aerosols on Earth's radiation field. Radiation arriving at the surface is extinguished as a function of the optical and physical characteristics of the aerosol. The difference between the absorption and subsequent emission by aerosols results in warming of the atmospheric layer where the absorbing particles are located. As a result of the interaction of sunlight with atmospheric aerosols as it passes through the atmosphere, the properties of the radiation reaching Earth's surface will be changed. According to Beer law, the change in radiation is as follows:

$$dL = \frac{-e(z)Ldz}{\cos \theta_0} = -eLmdz \quad \text{with } m = \frac{1}{\cos \theta_0} \quad (3.1)$$

where L is the solar radiance, e is the extinction coefficient and θ_0 is the angle of radiation arrival. Rearranging and integrating both sides, we have:

$$\log \left(\frac{L}{L_0} \right) = -\tau m \quad (3.2)$$

where L is the solar radiance at the surface, L_0 is the TOA radiance, and τ is the aerosol optical depth.

$$\tau = \int_0^\infty e(z)dz \quad (3.3)$$

that can be defined as a measure of the extinction of the sun's radiation by atmospheric aerosols. Solving Equation 3.2 for the arrival radiance L , we obtain the Beer-Lambert law:

$$L = L_0 e^{-\tau m} \quad (3.4)$$

The optical thickness of an aerosol depends on the wavelength of light according to a power law known as Ångström's law

$$\tau(\lambda) = \beta \lambda^{-\alpha} \quad (3.5)$$

where β is the turbidity coefficient referred to as $1\mu m$ and is related to the aerosol column burden, α is the Ångström exponent (wavelength exponent) which is closely related to the aerosol-size distribution of the scattering particles: the smaller the particles, the larger the exponent. In addition to being a useful tool for extrapolating AOD throughout the shortwave spectral region, the Ångström exponent is also a qualitative indicator of aerosol particle size. Junge (1955) was the first to explore the relationship between the Ångström exponent and poly-disperse aerosol size distributions. Careful measurements observed that particle number concentration N versus particle radius r follows a similar power law function over a wide range of radii, known as the Junge distribution of atmospheric aerosols:

$$\frac{dN(r)}{d(\log r)} = Ar^{-\nu} \quad (3.6)$$

where A is a constant depending on the number of particles in one cubic centimeter and ν is the slope of the curve with a value ranging typically from 2-5. Subsequent research has shown that the Junge distribution does not accurately describe aerosol size distributions, and that they are better represented as multi-modal log-normal distribution, such that

$$\frac{dV(r)}{d \ln r} = \sum_{i=1}^n \frac{C_i}{\sqrt{2\pi}\sigma_i} \exp\left\{-\frac{(\ln r - \ln R_i)^2}{2\sigma_i^2}\right\} \quad (3.7)$$

where C_i represents the particle volume concentration, R_i is the median or geometric mean radius, σ_i is the variance or width of each mode and n is the number of log-normal aerosol modes. Due to the optical effects of atmospheric aerosols being more closely related to their volume then their number, the volume concentration has replaced the number density. These quantities are related as follows:

$$\frac{dV(r)}{dN(r)} = \frac{4}{3}\pi r^3 \quad (3.8)$$

The Ångström exponent remains, however, a good indicator of the fraction of small particles of radius $0.057 - 0.21\mu m$ relative to larger particles of radius $1.8 - 4\mu m$ for tropospheric aerosols.

A sun-sky radiometer is a narrow band filter photometer able to perform measurements of direct solar and diffuse irradiances at some selected wavelengths and several scattering angles. One way this is done is by using direct solar radiation measurements. The attenuation of the signal due to the properties of the material through which the light is travelling is given by the Beer-Lambert law (Equation 3.4):

$$V = V_0 e^{-\tau m_0} \quad (3.9)$$

where V is the signal at the ground, V_0 is the signal at the top of the atmosphere (TOA), m is the optical mass considering the solar zenith angle μ_0 ($1/\cos \theta = 1/\mu_0$) and τ is the total extinction optical depth (Equation 3.3) considering the molecular, aerosol and gas contribution.

Data from photometer measurements during February 11-12 and April 1, 8 and 17, 2020 in Rome, Italy are subsequently analyzed. Calculated values for aerosol optical depth, radius and volume were provided. Wavelength channels measure by the photometer are $0.34, 0.4, 0.5, 0.675, 0.87$ and $1.02\mu m$. AOD values at each band for each of the five days are shown in Figure 3.1. AOD values for April 8 are significantly higher at smaller wavelengths, with February 11 and April 17 having the highest values at longer wavelengths. AOD values for February 12 and April 1 are consistently lower than other days across all wavelengths.

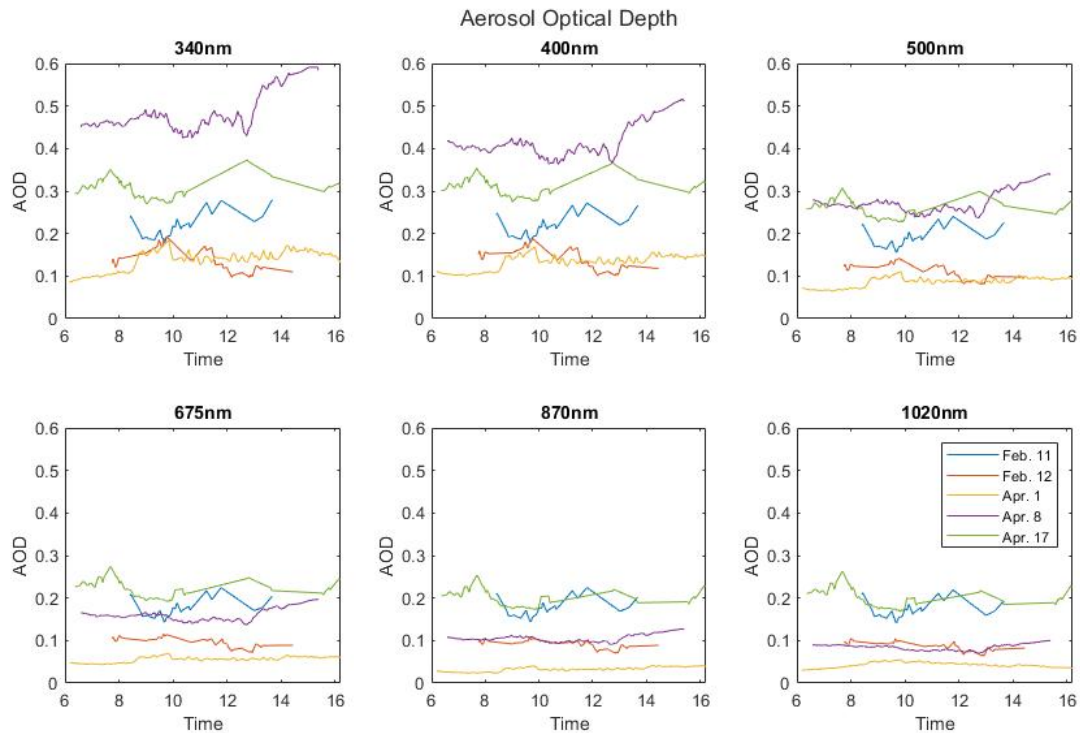


Figure 3.1: Aerosol optical depth for February 11-12 and April 1, 8 and 17, 2020 in Rome, Italy for each of the six bands: $0.34, 0.4, 0.5, 0.675, 0.87$ and $1.02\mu m$.

Taking the natural log of the wavelength versus the natural log of the AOD at a specific time and applying a linear fit, the Ångström exponent can be extrapolated from the slope. A scatter plot of $\ln(\text{AOD})$ vs $\ln(\lambda)$ at approximately 10:00 for the five days is shown in the left panel of Figure 3.2. Comparing the slopes for the different days, we see the slope for April 1 and 8 are much larger than that of the other days, which shows that for a particular value of AOD can correspond to a different situation in terms of aerosol composition inside the atmosphere. Taking the slope of a linear fit at each time interval, the Ångström exponent can be calculated for each day as shown in the right panel of Figure 3.2. Comparing the values of Ångström exponent for the five days, the values on April 1 and 8 show the atmospheric aerosols are composed of a larger amount of smaller particles.

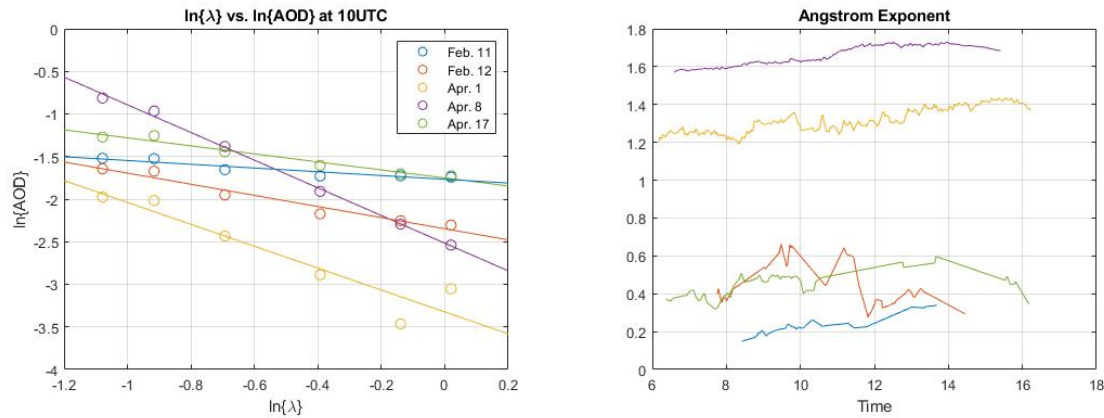


Figure 3.2: Calculated Ångström exponent for the five dates: (left) at approximately 10UTC and (right) for all time intervals.

Comparing the cases of AOD at 500nm vs Ångström exponent, we have high AOD with large Ångström exponent (April 8) suggesting the size distribution is dominated by the fine mode ($r < 0.5\mu\text{m}$), high AOD with low Ångström exponent (April 17) suggesting a size distribution is dominated by coarse mode ($r > 0.5\mu\text{m}$), low AOD with mid-high Ångström exponent (April 1) suggesting a relatively even distribution of fine and coarse mode particles. February 11-12 exhibit mid-low AOD with comparatively low Ångström exponent, which also suggest dominant coarse mode. These expectations from the AOD vs Ångström exponent can be compared to the size distribution calculation in Figure 3.3, which shows volume vs radius distribution for the five days at two daytimes. In the first case of April 8, the expectation is confirmed in that the fine mode dominates with an order of magnitude difference between the fine and coarse mode. The case of April 17, high AOD with low Ångström exponent shows order of magnitude higher coarse mode than fine mode. April 1 shows a relatively even distribution between fine and coarse modes, and February 11-12 shows coarse the coarse mode is dominate, as expected.

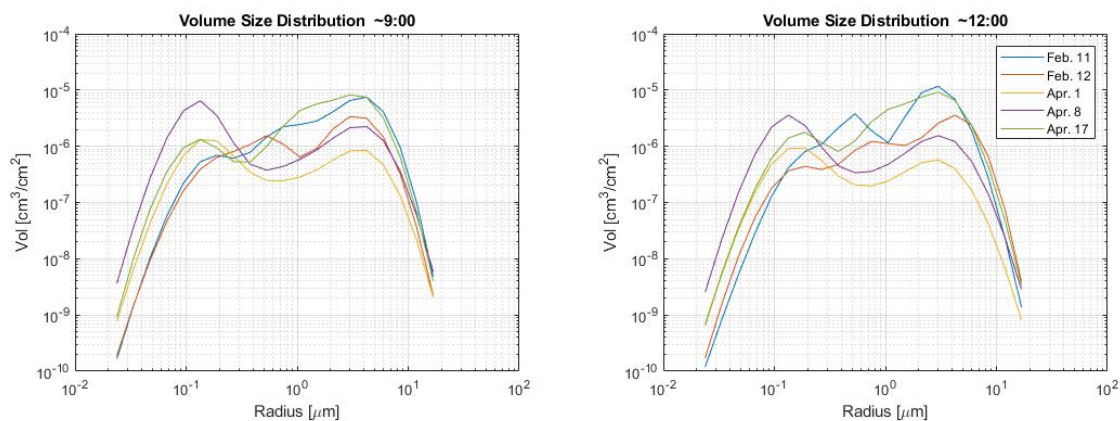


Figure 3.3: Volume size distribution for the five days at 9:00 and 12:00.

In order to understand the differences in the values previously analyzed among the five days, it is important to observe the where the air masses were coming from by analyzing the backwards trajectories. By obtaining a historic path the observed air masses, we can attempt to determine the origin of the relative aerosol contributions to the air masses. Figure 3.4 shows the NOAA HYSPLIT model 72h backward trajectories ending on April 1, 8 and 17 at 41.902N, 12.516E. There is a distinct difference in origin of the air masses arriving on the days, with

April 1 and 8 air masses coming from the north and through east Europe on April 8, compared to that of April 17 air mass coming from over Africa. In the case of April 17, transport of Saharan dust contributes the observed dominant coarse mode with high AOD and low Ångström exponent. Checking the satellite derived active fire data during the time period April 1-9 as is shown in Figure 3.5, which shows a significant number of active fires in the regions through which the air masses travelled arriving April 1 and 8. Biomass burning during these dates contributes the dominant fine mode with high AOD (shorter wavelengths) and high Ångström exponent.

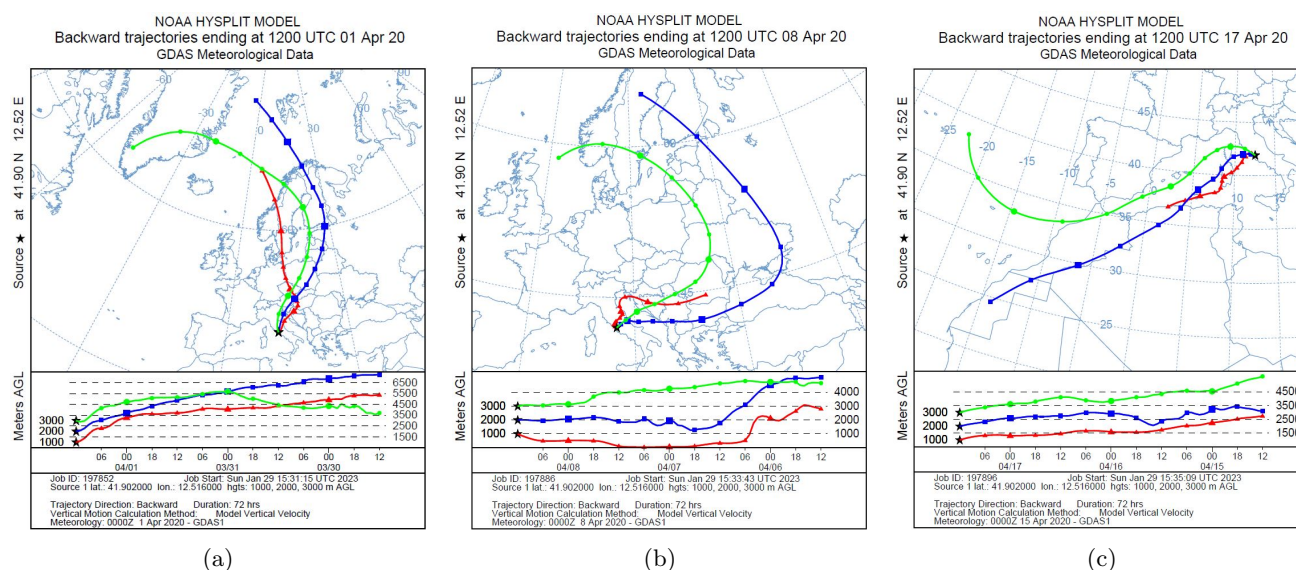


Figure 3.4: HYSPLIT 72h backwards trajectories for April 1, 8 and 17, 2020 arriving at 41.902N, 12.516E.

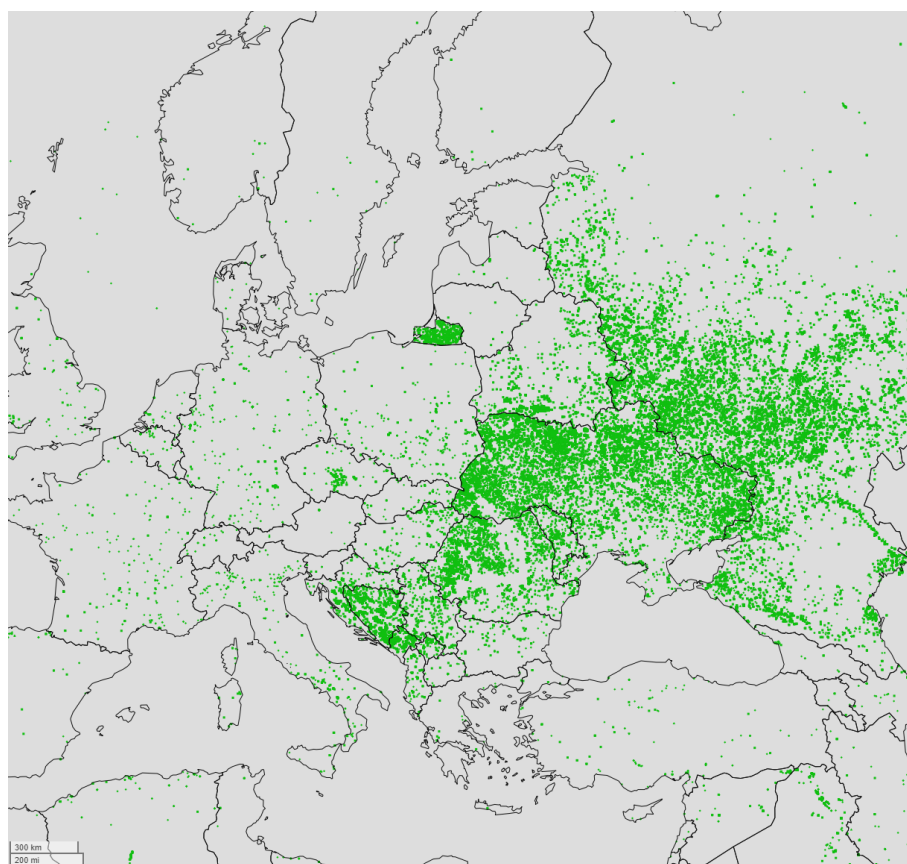


Figure 3.5: Active fires from April 1-9 derived from satellite observations found at https://effis.jrc.ec.europa.eu/apps/effis_current_situation/index.html. Green dots indicate an active fire during the time period.